

High geomagnetic field intensity recorded by anorthosite xenoliths requires a strongly powered late Mesoproterozoic geodynamo

Yiming Zhang^{a,1}, Nicholas L. Swanson-Hysell^a, Margaret S. Avery^{a,b}, and Roger R. Fu^c

^aDepartment of Earth and Planetary Science, University of California, Berkeley, CA, 94720; ^bGeology, Minerals, Energy, and Geophysics Science Center, U.S. Geological Survey, Moffett Field, CA, 94025; ^cDepartment of Earth and Planetary Sciences, Harvard University, Cambridge, MA, 02138

This manuscript was compiled on January 28, 2022

1 **Obtaining estimates of Earth's magnetic field strength in deep time**
2 **is complicated by non-ideal rock magnetic behavior in many igneous**
3 **rocks. In this study, we target anorthosite xenoliths that cooled**
4 **and acquired their magnetization within ca. 1092 Ma shallowly em-**
5 **placed diabase intrusions of the North American Midcontinent Rift.**
6 **In contrast to the diabase which fails to provide reliable paleointen-**
7 **sity estimates, the anorthosite xenoliths are unusually high-fidelity**
8 **recorders yielding high-quality, single-slope paleointensity results**
9 **that are consistent at specimen and site levels. An average value**
10 **of ~89 ZAm² for the virtual dipole moment from the anorthosites**
11 **with the highest site-level values up to ~140 ZAm² are higher than**
12 **that of the dipole component of Earth's magnetic field today and rival**
13 **the highest values in the paleointensity database. Such high inten-**
14 **sities recorded by the anorthosite xenoliths require the existence of**
15 **a strongly powered geodynamo at the time. Together with previous**
16 **paleointensity data from other Midcontinent Rift rocks, our new re-**
17 **sults indicate that a dynamo with strong power sources persisted for**
18 **more than 14 million years ca. 1.1 Ga. These data are inconsistent**
19 **with there being a progressive monotonic decay of Earth's dynamo**
20 **strength through the Proterozoic Eon and could challenge the hy-**
21 **pothesis of a young inner core.**

absolute paleointensity | Midcontinent Rift | anorthosite | geodynamo | Mesoproterozoic | inner core

1 Earth's magnetic field is the result of convective flow of
2 liquid iron-alloy in Earth's outer core. At present day,
3 the geodynamo is collectively powered by heat flow across the
4 core-mantle boundary (CMB) and from the crystallization of
5 the solid inner core from the liquid outer core which provides
6 latent heat and compositional buoyancy (1). However, while
7 paleomagnetic studies have found that a dynamo field has
8 existed since at least 3.4 billion years ago (2–4), Earth's inner
9 core likely crystallized more recently. Estimates of the timing
10 of the initial crystallization of Earth's inner core are inter-
11 connected with estimates for the core's thermal conductivity.
12 Higher conductivity values imply faster cooling rates, which in
13 turn imply that the threshold for the freezing of the inner core
14 happened more recently (5). While some estimates of these
15 values are consistent with an inner core age >3 Ga (6, 7), other
16 estimates have implied higher thermal conductivity values and
17 an age for the inner core that is less than 1.3 Ga (8–11), with
18 some suggesting even younger ages (<700 Ma; 12, 13). Given
19 that estimates for the core's thermal conductivity continue
20 to be debated, it is crucial to use observational records as an
21 independent constraint on the thermal evolution of Earth's
22 core and mantle.

Paleomagnetic records from ancient rocks are one of the few types of observational data that have the potential to provide

25 constraints on the thermal evolution of Earth's core. Evidence
26 for a persistent magnetic field through the Proterozoic, for
27 example, likely necessitates the existence of plate tectonics
28 that sustained core-mantle boundary heat flow (14). However,
29 strikingly low estimates of geomagnetic field strengths have
30 been obtained ca. 565 Ma during the Ediacaran Period (15–
31 17) and ca. 370 Ma during the Devonian Period (18–20),
32 potentially indicating unusual periods of core dynamo regime
33 at those times. The Ediacaran data have been interpreted to
34 indicate that there was a progressively decaying field up to
35 that time that was followed soon after by initial crystallization
36 of the inner core (15).

37 Determinations of the absolute value of ancient geomag-
38 netic field strength rely on igneous rocks that acquire thermal
39 remanent magnetizations as they cool. These magnetizations
40 need to be unmodified by subsequent heating or chemical alter-
41 ation in order to maintain a record of the ancient geomagnetic
42 field from the time of cooling. Intracontinental magmatic
43 events are therefore an important target for determination of
44 ancient paleointensity as they can be well-preserved within
45 continental interiors. This interior position results in them

Significance Statement

Acquiring high-fidelity observational records of ancient mag-
netic field intensity from the remanent magnetization of rocks
is crucial for constraining the long-term evolution of Earth's
core. However, robust estimates of ancient field strengths are
often difficult to recover due to alteration or non-ideal rock mag-
netic behavior. In this study, we use plagioclase cumulates
(anorthosite) that formed in the deep crust and were brought to
the near surface by magma where they cooled and acquired
thermal remanent magnetizations. These anorthosite xenoliths
have experienced minimal alteration since their emplacement
and yield high quality paleointensity estimates. In contrast to
predictions of a progressively decaying field leading up to late
nucleation of Earth's inner core, these data record a strong
virtual dipole moment 1.1 billion years ago. A strong field per-
sisted over at least a 20-million-year interval indicating the
existence of appreciable power sources for Earth's dynamo
during the late Mesoproterozoic.

Author contributions: Y.Z. and N.L.S.-H. designed research; Y.Z., N.L.S.-H. and M.S.A conducted fieldwork and sampling; Y.Z. and N.L.S.-H. conducted and analyzed rock magnetic experiments; Y.Z. performed petrography and electron microscopy; R.R.F. contributed to magnetic imaging data analyses; Y.Z. and N.L.S.-H. wrote the paper with input from M.S.A. and R.R.F.

The authors declare no conflict of interest.

¹To whom correspondence should be addressed. E-mail: yimingzhang@berkeley.edu

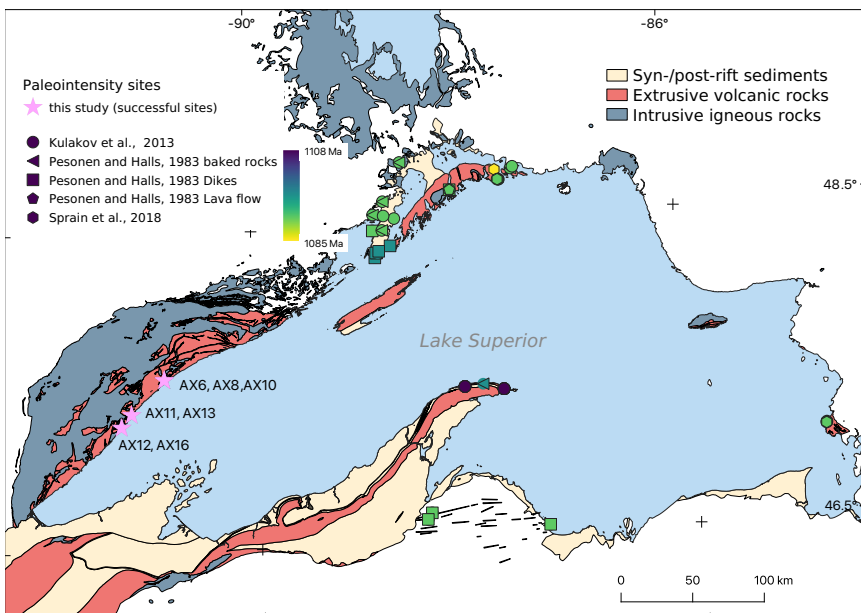


Fig. 1. Simplified geologic map of the Lake Superior region showing the distribution of rocks associated with the late Mesoproterozoic Midcontinent Rift. Purple stars mark sites with paleointensity results that passed the selection criteria from this study. Paleomagnetic sites from 21 are categorized by lithology. All sites from 21–23 are color-coded by their ages.

typically being distant from tectonic events along continental margins that can drive alteration through heat and fluids. However, intraplate magmatism associated with large igneous provinces is typically of geologically short duration with the bulk of magmatic products emplaced within 1 Myr or less (24). The Midcontinent Rift (Fig. 1) is an exception as it is a large igneous province where magmatism lasted ~25 Myr from ca. 1109 Ma to 1084 Ma (25). Additionally, extension ceased in the Midcontinent Rift prior to lithospheric separation, preserving volcanic, intrusive, and sedimentary rocks of the rift within the continental interior. As a result, rocks of the rift have unusually simple paleomagnetic behavior for their greater than one billion-year-old age and paleomagnetic data from rift rocks forms a central record of Mesoproterozoic paleogeography (14). The duration of magmatic activity within the Midcontinent Rift is longer than the entire 20.4 Myr long Neogene Period such that it enables an extended well-preserved window into the intensity of Earth's magnetic field in the late Mesoproterozoic.

Despite the excellent preservation of the rocks, non-ideal paleointensity behaviors have challenged the interpretation of many previous paleointensity results from the Midcontinent Rift (21–23). The most trusted type of paleointensity estimate is that obtained through experiments in which the primary natural thermal remanent magnetization is progressively replaced by a laboratory magnetization that is imparted in a known field with internal consistency checks (such as in IZZI-style Thellier experiments; 26). In such Thellier paleointensity experiments, one typical departure from ideal behavior is sagging or double-slopes as visualized in plots that show thermal remanent magnetization (TRM) acquired versus natural remanent magnetization (NRM) lost. For such data, distinct paleointensity estimates may be calculated depending on the interpreter's choice of slope. Typically, such non-ideal behavior would result in a higher paleointensity estimate from the steeper-sloped low-temperature portion and a lower paleointensity estimate from the high-temperature portion. For example, in data from the Midcontinent Rift, ref. 21 used the low-temperature slope as the best representation of the

past magnetic field strength (likely overestimating the field strength) whereas ref. 22 used the high-temperature slope (likely underestimating the field strength). Such non-ideal results were rejected by 23 who applied stricter paleointensity selection criteria, but as a result had few accepted sites.

In this study, we target a unique rock type—high-purity anorthosite xenoliths. Anorthosites are cumulate rocks composed dominantly of the mineral plagioclase. They are attractive targets for paleomagnetic study as plagioclase crystals can enshroud magnetic inclusions from alteration with alteration of the plagioclase crystals themselves not resulting in the formation of secondary iron oxides in contrast with mafic minerals such as olivine. The anorthosite xenoliths targeted in this study were brought to the near surface in magma that formed hypabyssal intrusions of the Beaver River diabase (27). They cooled and acquired their magnetizations in conjunction with the host diabase at a paleolatitude of $22^{\circ}\pm 2^{\circ}$ (calculated from the paleomagnetic pole of the coeval Portage Lake Volcanics; 25, 27). Paleointensity experiments on the anorthosite xenoliths have a high success rate, yielding consistent specimen- and site-level paleointensity results. Rock magnetic data reveal that the anorthosite xenoliths have low anisotropy of thermal remanent magnetization (TRM) and can acquire TRM linearly within relevant field strengths. Magnetic imaging shows the anorthosite specimens have dominant magnetic carriers within and interstitial to plagioclase crystals, and they do not display strong preferred orientations. These single-slope, high quality paleointensity data, together with other high-quality paleointensity records during the protracted Midcontinent Rift magmatic activity, require that there was a strong late Mesoproterozoic geodynamo.

Background on anorthosite xenoliths of the Beaver River diabase

While magmatic activity within the Midcontinent Rift was protracted, there were intervals of particularly rapid volcanism and voluminous emplacement of intrusions. The ca. 1092 Ma Beaver Bay Complex in northern Minnesota punctuates

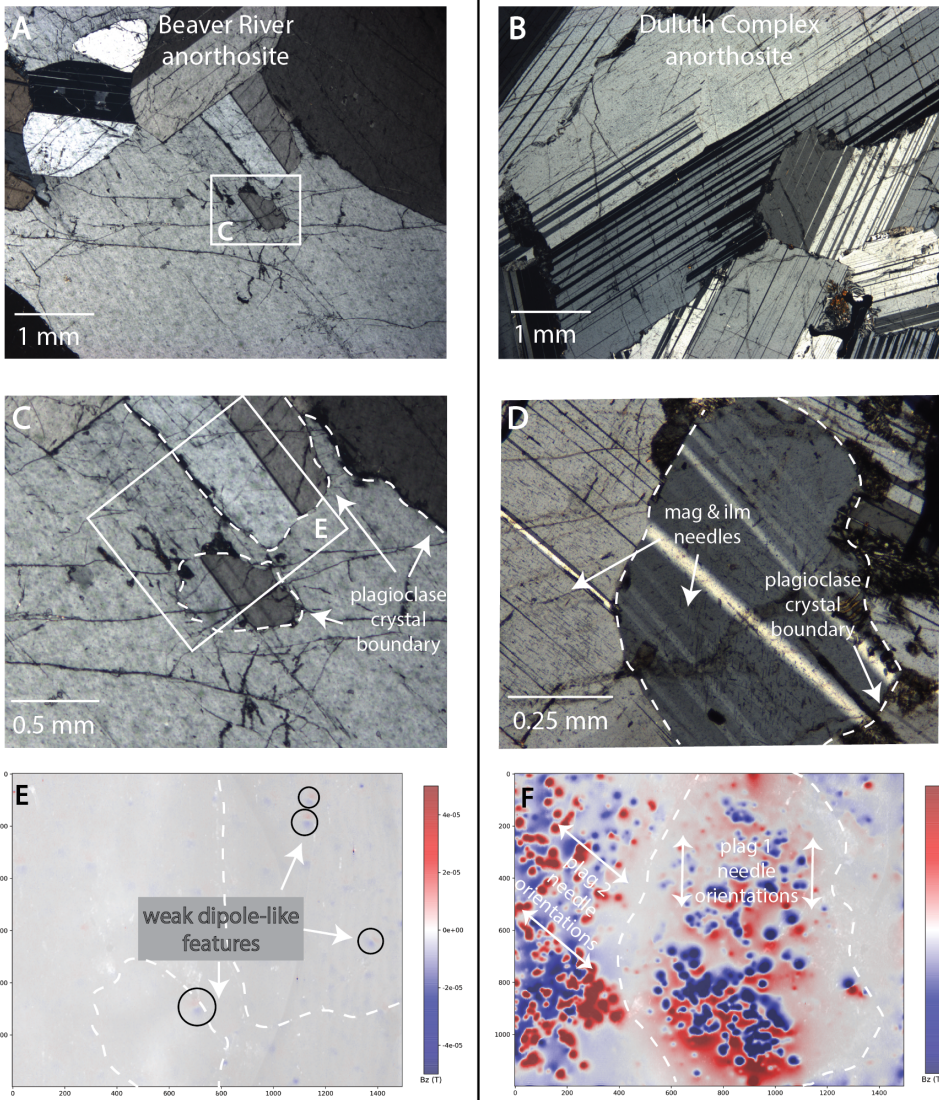


Fig. 2. Thin section petrographic images (A,B,C,D) and magnetic maps (E,F) of anorthosite from the Beaver River anorthosite xenolith from which paleomagnetic site AX16 and geochronology sample MS99033 were collected (left column; 27) and a distinct anorthosite from the Duluth Complex Anorthositic Series (right column). The Duluth Complex anorthosites were not targeted for paleointensity experiments in this study given the complexities associated with more pronounced fabrics. Cross-polarized petrographic images of the Beaver River anorthosite (A,C) reveal plagioclase with a granoblastic texture with crystals that are largely free of large opaque inclusions. In contrast, plagioclase crystals in the Duluth Complex anorthosite have euhedral, interlocking crystals with an igneous foliation (B) and the plagioclase crystals contain abundant Fe-Ti oxide needles that have preferred orientations that are often parallel with the [001] axis of the plagioclase. Magnetic field maps acquired with a quantum diamond microscope (QDM) on samples to which an IRM has been applied show that the relatively weak magnetic sources within and interstitial to plagioclase crystals exist in the Beaver River anorthosite in (E) while large oxide needles within Duluth Complex plagioclase are strongly magnetic as evidenced through the overlapping magnetic fields above the oxides in (F). Magnetic field maps of (E) and (F) share the same spatial and magnetic scale. The unit of the axes are in μm .

one such period of magmatism during the main stage of Mid-continent Rift activity. The magma that formed the 1091.7 \pm 0.2 Ma Beaver River diabase dikes and sills of the Beaver Bay Complex transported numerous anorthosite xenoliths that have short-axis diameters up to 180 meters via wide conduits (28, 29). These anorthosite xenoliths are plagioclase cumulates that formed comagmatically with the host diabase in the lower crust—an interpretation confirmed by U-Pb zircon geochronology (27).

Thermal modeling results and paleomagnetic directional data show the anorthosite xenoliths to have acquired thermal remanent magnetizations while cooling with the Beaver River diabase (27). Step-wise thermal demagnetization data show the anorthosite xenoliths to have dominantly single-component magnetization that often unblock sharply within temperature ranges between 500°C and 580°C, consistent with magnetization held by low-titanium titanomagnetite (27).

Results and Interpretations

Petrography and magnetic imaging of anorthosite xenoliths

The dominantly monomineralic anorthosite xenoliths within

the Beaver River diabase often have granoblastic texture characterized by equigranular crystals with weakly developed petrofabrics (Fig. 2A). In addition, the plagioclase crystals of the anorthosite xenoliths are typically free of large oxide inclusions (Fig. 2C). Magnetic imaging using a quantum diamond microscope (QDM) shows that the dominant magnetic remanence carriers often exist within, and sometimes interstitial to, plagioclase crystals (Fig. 2E).

These features of the Beaver River anorthosite xenoliths are distinct from many other anorthosites such as the anorthosite xenoliths within the Duluth Complex Anorthositic Series rocks—older intrusions within the Midcontinent Rift. To illustrate these differences, we present petrographic and magnetic imaging data from a sample of Duluth Complex anorthosite that was not targeted for paleointensity experiments. The plagioclase of the Duluth Complex anorthosites typically develop interlocking textures that display strong igneous foliation (Fig. 2B). In addition, there are abundant Fe-Ti oxide needles that are typically aligned with the [001] axes of the plagioclase crystals (Fig. 2D). Magnetic imaging confirms that these strongly magnetic needles within the plagioclase crystals often have magnetic moments oriented along their long axes (Fig. 2D,F).

164 Titanomagnetite and ilmenite symplectitic intergrowths also
 165 coexist with pyroxene and relict olivine as a product of olivine
 166 oxidation in the Duluth Complex magma (30).
 167 The lack of symplectites and the lack of large plagioclase-
 168 hosted titanomagnetite needles within the Beaver River
 169 anorthosite xenoliths targeted in this study distinguish them
 170 from plagioclase cumulates of the Duluth Complex and other
 171 layered mafic complexes where anisotropic magnetic mineral
 172 fabrics associated with igneous foliation often occur (31–33).
 173 The relative lack of fabric and associated preferred orientation
 174 makes the Beaver River anorthosite xenoliths a particularly
 175 compelling target for paleointensity experiments.
 176 **Paleointensity.** Following IZZI-style paleointensity experi-
 177 ments (26), 40 from a total of 86 anorthosite specimens and 0
 178 out of a total of 69 diabase specimens passed our paleointensity
 179 result selection criteria (see Materials and Methods section).
 180 7 anorthosite sites and no diabase site-level results pass these
 181 selection criteria. Example NRM/TRM (Arai) plots are shown
 182 in Figure 3. Summary specimen absolute paleointensity es-
 183 timates and site-level mean paleointensity values are plotted
 184 in Figure 4 (and provided in Table S1). The paleointensity
 185 quality index (Q_{PI} ; 34) for the anorthosite xenoliths are all
 186 5 or 6 (Table S2). The cooling rate-corrected absolute paleo-
 187 intensity estimates from all anorthosite sites have a mean of
 188 $38.28 \pm 11.92 \mu\text{T}$. This paleointensity value corresponds to a
 189 calculated virtual dipole moment of $\sim 89 \text{ ZAm}^2$ (10^{21} Am^2) ca.
 190 1092 Ma. All measurement-level paleointensity experiment
 191 data are available within the MagIC database (<https://earthorg/MagIC/19462/8d3c2258-11ae-4830-b99f-3f6b02eceb7e>; *this private link is provided for the purpose of review; the url will be updated when a doi is generated for this manuscript*).
 192 Typical paleointensity experimental data of the anorthosite
 193 specimens have straight, single-slope NRM/TRM plots and
 194 the accepted fractions of temperature steps span over the
 195 origin-trending, primary remanence components (Fig. 3). We
 196 accept specimen- and site-level absolute paleointensity results
 197 from those anorthosite xenoliths that pass the selection crite-
 198 ria. Other anorthosite xenoliths and diabase specimens failed
 199 the selection criteria largely because of double-slope or sagging
 200 behavior (fail FRAC selection; see Materials and Methods sec-
 201 tion), poor pTRM checks, and sometimes zigzagging behaviors
 202 superimposed on top of sagging behavior (fail SCAT, DANG
 203 selection; see Materials and Methods section; Fig. 3). A 20
 204 mT alternating field treatment after in-field heating steps was
 205 applied to some specimens, but it did not result in significant
 206 changes in the experimental results for the anorthosite xenolith
 207 or diabase specimens (Fig. 4; Supporting Information).
 208 In addition to estimating paleointensity values by introduc-
 209 ing a set of selection criteria to filter our experiment results,
 210 we apply an independent method of 35 which uses all exper-
 211 imental data regardless of their NRM/TRM plot statistics to
 212 perform bias corrected estimation of paleointensity (BiCEP).
 213 This Bayesian probabilistic method is based on an assumption
 214 that paleointensity estimates from specimens that come from
 215 a same cooling unit are distributed around a true paleointen-
 216 sity value with the various deflections being expressed as
 217 the curvature parameter of the NRM/TRM plot (36). The
 218 posterior paleointensity distributions from these sites with
 219 high-quality specimen-level data are in agreement with the
 220 site-level averages developed using the selection criteria ap-
 221 proach (Fig. 4; Fig. S1). Overall, the high-quality results from
 222 the anorthosite xenoliths of the Beaver River diabase indicate
 223 that the anorthosite xenoliths record a high geomagnetic field
 224 ca. 1092 Ma.
 225 **Rock magnetism.** Rock magnetic data support that the
 226 anorthosite specimens that pass the paleointensity selection
 227 criteria have dominant magnetic remanence carriers with mag-
 228 netic properties similar to stoichiometric, non-interacting, sin-
 229 gle domain magnetite, whereas anorthosite samples that failed
 230 the paleointensity result selection and all diabase samples have
 231 more pronounced populations of non-ideal carriers. Magnetic
 232 property measurement system (MPMS) data show both dia-
 233 base and anorthosite contain (titano)magnetite as evidenced
 234 through the presence of the Verwey transition (Fig. S2; 37, 38).
 235 Anorthosite specimens from sites that yield successful paleo-
 236 intensity results have Verwey transition temperatures near
 237 120 K as expected for stoichiometric magnetite with minimal
 238 Ti (39). However, diabase and anorthosite specimens that did
 239 not pass our paleointensity selection typically have Verwey
 240 transitions that are suppressed toward lower temperatures
 241 (Fig. S2), indicating that magnetite grains in the specimens
 242 either have relatively higher Ti content or have been partially
 243 oxidized (39).
 244 Coercivity spectra from backfield experiments further sup-
 245 port the interpretation that rocks that pass or fail the se-
 246 lection criteria have distinct magnetic mineralogy (Fig. 5).
 247 A compilation of median destructive field (MDF) values in
 248 Figure 5 shows that specimens from anorthosites that pass
 249 paleointensity selection criteria have distinctly higher average
 250 MDF values than other anorthosite and diabase specimens.
 251 Single-component fits for coercivity spectra (40) show that
 252 anorthosites that yielded successful paleointensity results can
 253 have magnetic grain populations with peak coercivity around
 254 80 mT (Fig. 5). In contrast, other anorthosite and diabase
 255 tend to have lower peak coercivities (~ 30 mT). This result is
 256 consistent with an interpretation that a population of magnetic
 257 grains with more multidomain-like behavior is responsible for
 258 the non-ideal paleointensity behaviors during experiments on
 259 such specimens.
 260 **TRM anisotropy and nonlinear acquisition check.** Significant
 261 remanence anisotropy has been documented to exist within
 262 certain anorthositic rocks that form in layered intrusive com-
 263 plexes (32, 33). Strong remanence anisotropy associated with
 264 the igneous foliation developed within anorthosite from the
 265 Stillwater Complex has been shown to lead to significant overes-
 266 timation or underestimation of paleointensity values depending
 267 on the relative orientations between the fabrics and an ap-
 268 plied magnetic field (32). To assess whether our paleointensity
 269 estimates are biased by remanence anisotropy, we calculated
 270 the gamma statistic, which is the angular difference between
 271 the last pTRM step of paleointensity experiment and the ap-
 272 plied field direction. The results show that the anorthosite
 273 specimens used for paleointensity experiment have low gamma
 274 values ranging from 0.9° to 11.9° , with a median value of
 275 4.2° (Table S1). These gamma values are similar to those of
 276 Midcontinent Rift volcanics (23). Therefore, the Beaver River
 277 anorthosite xenolith bulk samples do not have significant rema-
 278 nence anisotropy. Paleodirectional data from our anorthosite
 279 xenoliths further support that they have minimal remanence
 280 anisotropy as their site mean directions closely match those
 281 of the Beaver River diabase hosts without deviating due to
 282
 283
 284

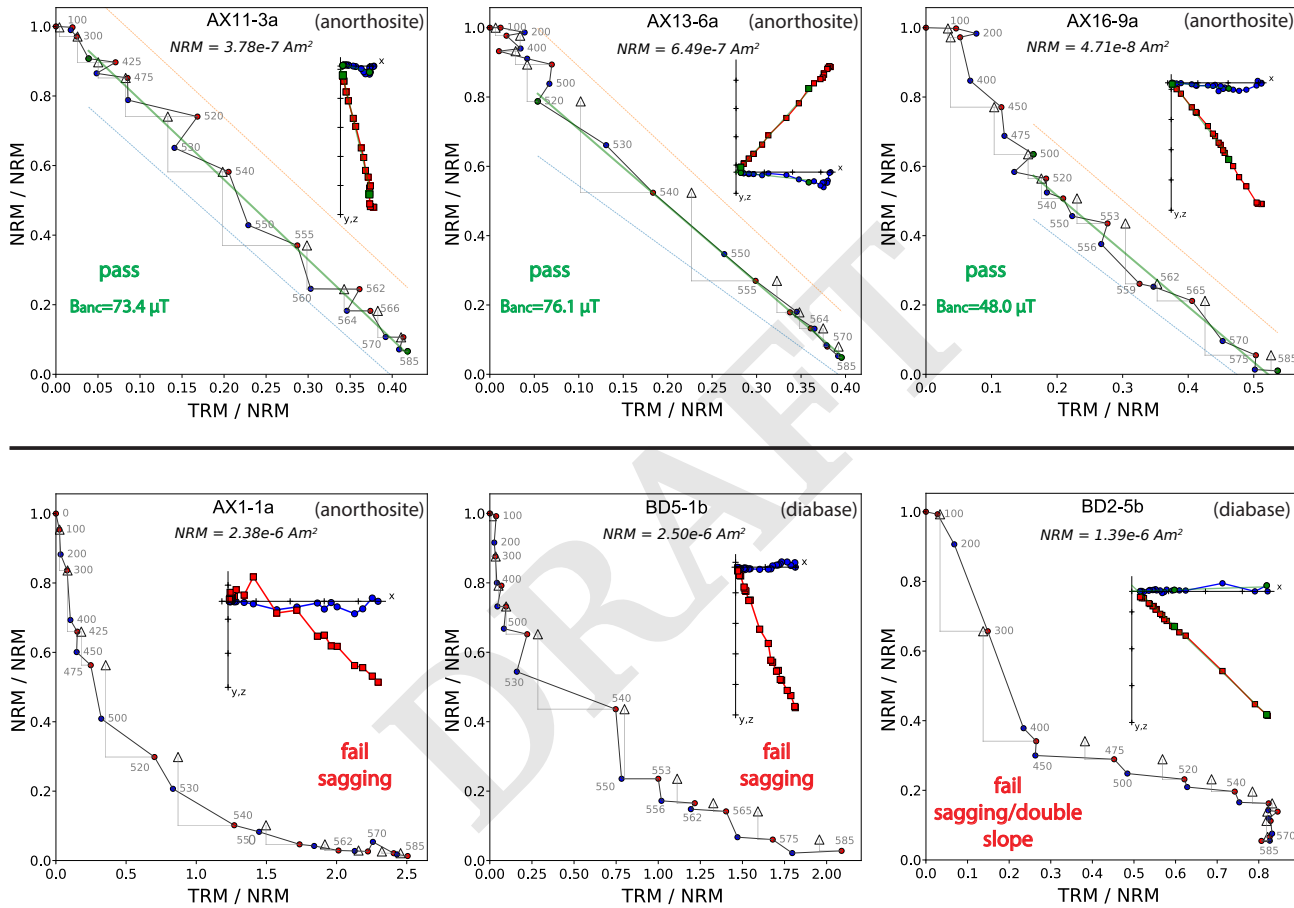


Fig. 3. Example results of paleointensity experiments are displayed on Arai plots and zero-field heating results are shown on inset orthogonal plots (Zijderveld plots) for anorthositic and diabase specimens. Red (blue) circles indicate zero-field/in-field (in-field/zero-field) steps 'ZI' ('IZ'). Triangles mark partial thermal remanent magnetization (pTRM) checks. Blue and red squares in the Zijderveld plots are X-Y and X-Z projections, respectively, of the NRMs in specimen coordinates. Plots on the top row show successful specimen paleointensity results with straight, single-slope behaviors that pass our selection criteria. The green lines represent fits for the dominant single-slope component that passes the acceptance criteria and gives an estimate of the ancient field strength (B_{anc}). The plots for anorthositic specimens AX1-1a and diabase BD5-1b on the bottom row show typical non-ideal sagging behaviour that fails our acceptance criteria. Specimen BD2-5a is an example where the data appear linear with distinct slopes in the low and high temperature ranges such that it could pass less restrictive selection criteria, particularly if a narrower temperature range was used for the experiment.

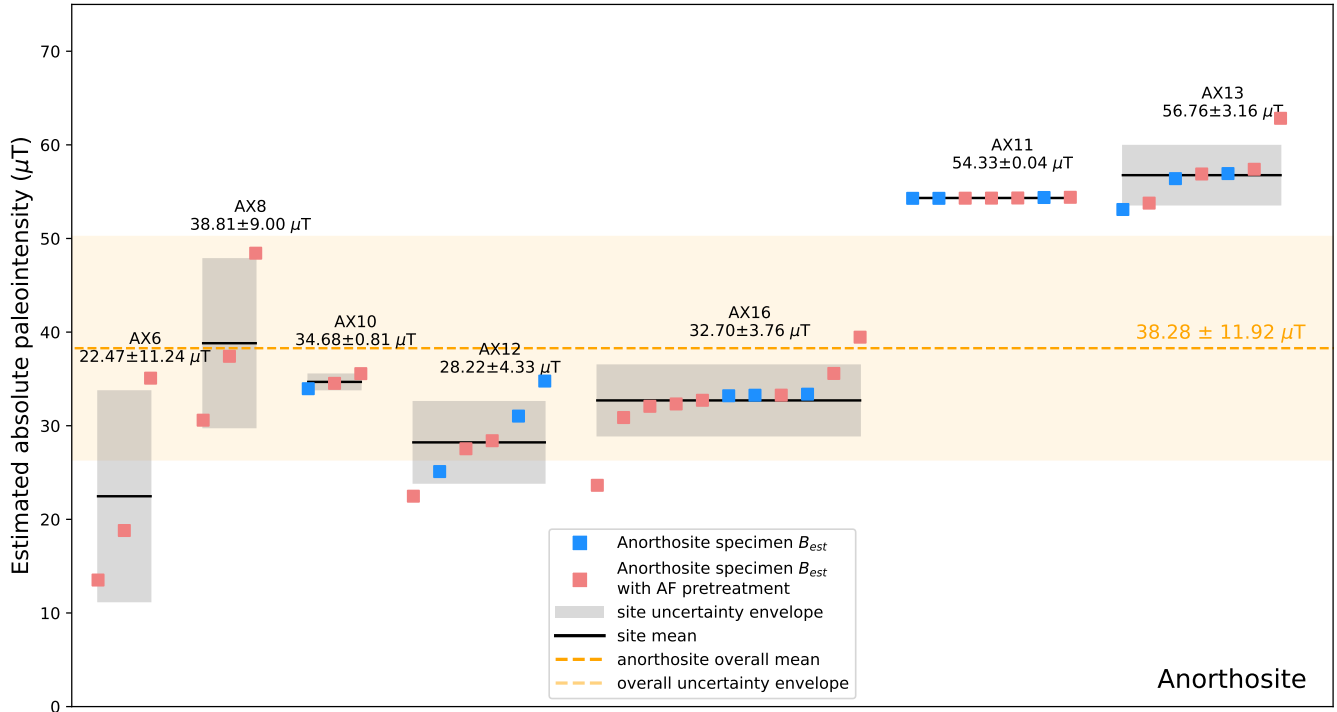


Fig. 4. Summary plot of individual specimen absolute paleointensity results (square symbols) from this study and their averages and standard deviations at site (black bars with grey uncertainty boxes) and locality level (orange dashed line and bar). All results are corrected for cooling rate with a factor of 0.74.

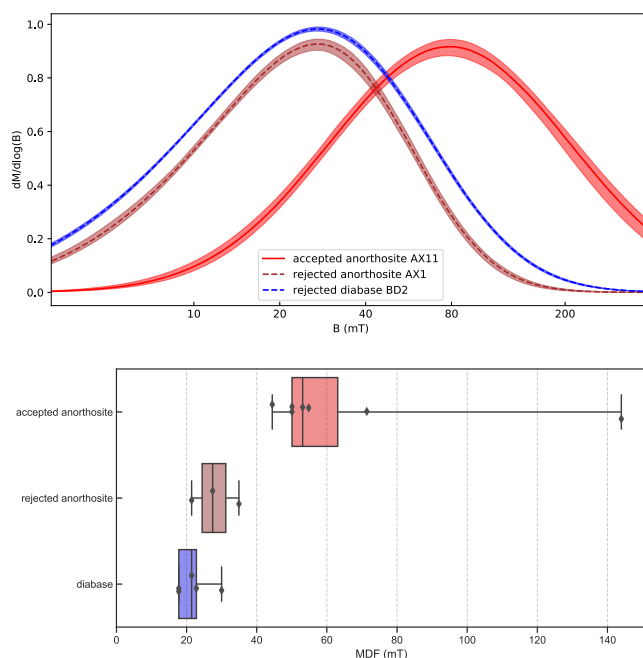


Fig. 5. Top: Example coercivity spectra of anorthosite and diabase specimens from sites that pass or fail our paleointensity selection criteria. Bottom: Box plots of median destructive field (MDF) values for all anorthosite and diabase specimens with single-component coercivity unmixing results. Both plots show that anorthosite specimens that pass paleointensity selection criteria have higher coercivities consistent with a higher portion of single-domain-like magnetite grains than the other anorthosite specimens and the diabase.

a fabric (27). In addition, no resolvable magnetic fabric was observed in the anorthosite xenoliths through petrographic and magnetic imaging (Fig. 2).

We applied full TRMs to a set of anorthosite specimens with lab fields of 30, 50, 70, and 90 μT along specimen vertical axes. The results show that this set of anorthosite specimens did not saturate upon the applied fields and there is thus no need for correcting nonlinear thermal remanence acquisitions (2; Fig. S4).

Considering secular variation and cooling rate. To best characterize the geomagnetic axial dipole field intensity during a certain time period a paleointensity dataset should cover a sufficient amount of time such that paleosecular variations of the geomagnetic field are averaged. Thermal modeling results from ref. 27 suggest that the Beaver River anorthosite xenoliths were heated to tholeiitic magma temperature ($\sim 1100^{\circ}\text{C}$) and acquired thermal remanent magnetization during cooling with their diabase host on a time scale of a thousand years, partially averaging secular variation within single sites. Anorthosite xenoliths have paleointensity results that are consistent within small regions, but vary between localities. Anorthosite AX12 and AX16 were emplaced ~ 450 meters apart and have very similar paleointensity estimates (Figs. 1 and 4). ~ 10 km to the north, anorthosite xenoliths AX11 and AX13 were also emplaced closely (separated by ~ 125 meters) and yield similar values to one another but distinct paleointensity estimates from those of AX12 and AX16 (Figs. 1 and 4). The data therefore capture different intervals of time during the emplacement and cooling of the Beaver River diabase sills ca. 1092 Ma.

Another consequence of the anorthosite xenoliths having

cooled in the interior of thick diabase intrusions is that slow cooling rates can bias paleointensity estimates toward higher values. Large differences in cooling rates between acquisition of an NRM in nature versus a TRM in the lab can result in overestimated paleointensities for single domain grains (41–43). From the thermal history model of ref. 27, we can estimate the duration over which the diabase and anorthosite cooled from the Curie temperature of magnetite ($\sim 580^\circ\text{C}$) to the time when they fully blocked in their characteristic natural remanence magnetization ($\sim 500^\circ\text{C}$; 27). We find the cooling time to be on the order of ~ 1 kyr, which corresponds to a cooling rate of $\sim 1.6 \times 10^{-9} \text{ }^\circ\text{C s}^{-1}$. In contrast, the lab cooling rate is much faster through the same temperature interval with an estimated cooling rate of $\sim 1.3 \times 10^{-1} \text{ }^\circ\text{C s}^{-1}$. The significant cooling rate difference leads to a predicted $\sim 36\%$ overestimate of true ancient field following the model of 42 (Fig. S3). This estimate on cooling rate effect is similar to the value of $\sim 35\%$ overestimate derived from the model of ref. 43. We therefore correct our paleointensity results by a factor of 0.74. The cooling rate-corrected specimen paleointensity estimates together with specimen- and site-level means are shown in Fig. 4.

Discussion

The crystallization of the solid inner core is an important event in the long-term evolution of Earth's core and in sustaining the geodynamo (1). The age of the inner core in thermal evolution models relies on estimates for the thermal conductivity of iron alloys at the temperatures and pressures of the core (48). Prior to studies in the last 10 years, an accepted value of $\sim 30 \text{ W m}^{-1} \text{ K}^{-1}$ for this thermal conductivity was used to constrain the timing of inner core nucleation to be during the first half of Earth history (7, 49). Subsequently, experimental data and *ab initio* simulations were interpreted to imply higher thermal conductivity values (8, 13) which in turn imply a younger age of the inner core ($< 700 \text{ Ma}$; 12). However, other experimental studies continue to indicate lower thermal conductivity values consistent with prior estimates (7, 50) with no consensus yet emerging (48, 51). These experiments are challenging to conduct and interpret given complexities such as constraining the sample thickness under high pressure and temperature conditions, the validity of applying the Wiedemann-Franz law to extrapolate thermal conductivity values based on electrical resistivity measurements (13), and modeling uncertainties associated with parameters used in direct thermal conduction measurement experiments (7). Further experiments and theory are needed to explain these contrasting results which at present leave open very different trajectories for Earth's thermal evolution. As a result, the age of the inner core is relatively unconstrained from a theoretical perspective.

The other data type that can provide insight into the long-term history of the core's thermal regime and geodynamo is paleomagnetic data—both paleodirectional data that indicate the presence of a geomagnetic field and paleointensity data that constrain the field's strength. Inner core nucleation would have increased the power to the geodynamo which has the potential to manifest as an increase in Earth's surface field (52). An approach combining dynamo simulations and theoretical scaling relationships has predicted that progressive decay of the field's dipole moment would be followed by a rapid increase in geomagnetic field intensity soon after the onset of inner core

nucleation such that there is a minimum in dipole moment just before inner core nucleation (52). Other scenarios are possible, however, such as the prediction that while power increases associated with inner core nucleation would result in increases in Earth's internal magnetic field strength, the dynamo would also become more deeply seated in the core, diminishing the increase in observed magnetic field at Earth's surface (53, 54). Observational paleomagnetic records hold the potential for testing different model predictions and identifying transitions in ancient field strength (15, 55).

It has been proposed that Proterozoic paleointensity data are consistent with a progressive monotonic decay leading up to ca. 565 Ma in the Ediacaran Period (Fig. 6; 15). This interpretation was motivated by paleointensity estimates developed from the ca. 565 Ma Sept-Îles layered mafic intrusive complex of $\sim 7 \text{ ZAm}^2$ that are among the lowest values in the paleointensity database (Fig. 6; 15). A decay in the lead-up to this time was argued to be consistent with an absence of an inner core and a dynamo to which progressively less power was available through secular cooling (15, 52). This timing of inner core formation would favor a high core thermal conductivity (e.g. 13). Paleomagnetic directional excursions (56), other weak paleointensity estimates (17), and frequent polarity reversals (57) in rocks of similar age are interpreted to be consistent with numerical simulations (58) associated with a weak dipole field.

The high paleointensity estimates from the 1.1 billion-year-old Midcontinent Rift rocks challenge the hypothesized monotonic decay of the strength of the geomagnetic field throughout the Proterozoic Era. Instead, the well-preserved ca. 1092 Ma anorthosite xenoliths of the Beaver River diabase record a strong geomagnetic field in the late Mesoproterozoic that exceeds the strength of the modern-day field for which crystallization of the inner core is a power source (Fig. 6). Together with previous records obtained from the ca. 1106 Ma Osler Volcanics of the Midcontinent Rift (23), these data indicate that appreciable power to Earth's dynamo persisted through at least 14 Myr during the late Mesoproterozoic to maintain a strong surface field (Fig. 6). In addition to these high geomagnetic fields recorded by Midcontinent Rift rocks, the ca. 755 Ma Mundine Well dikes (46) also require a stronger geomagnetic field in the Neoproterozoic than would be predicted by a progressive Proterozoic decline (Fig. 6).

The hypothesis that a weak Ediacaran geomagnetic field is a telltale sign of the lack of an inner core with core nucleation following shortly thereafter may predict that it is the most significant weak to strong field transition in the paleointensity record. However, Fig. 6 shows that transitions from low to high field intensities occurred before, during, and after the Ediacaran. In the Ediacaran record developed to date, there is a two-fold increase in Earth's virtual dipole moment when comparing estimates from the ca. 565 Ma Sept-Îles intrusions (15) to those from ca. 550 Ma volcanics of the Skinner Cove Formation (47) (Fig. 6). In the late Mesoproterozoic, there is at least a six-fold increase within a period of ~ 35 Myr from a low average virtual dipole moment of $\sim 13 \text{ ZAm}^2$ recorded by the ca. 1140 Ma Abitibi dikes which yielded straight Arai plots (59), to a high moment of $\sim 70 \text{ ZAm}^2$ recorded by the ca. 1106 Ma Osler Volcanics, with even stronger values from ca. 1092 Ma by Beaver River anorthosite xenoliths that record virtual dipole moments up to $\sim 140 \text{ ZAm}^2$. While the

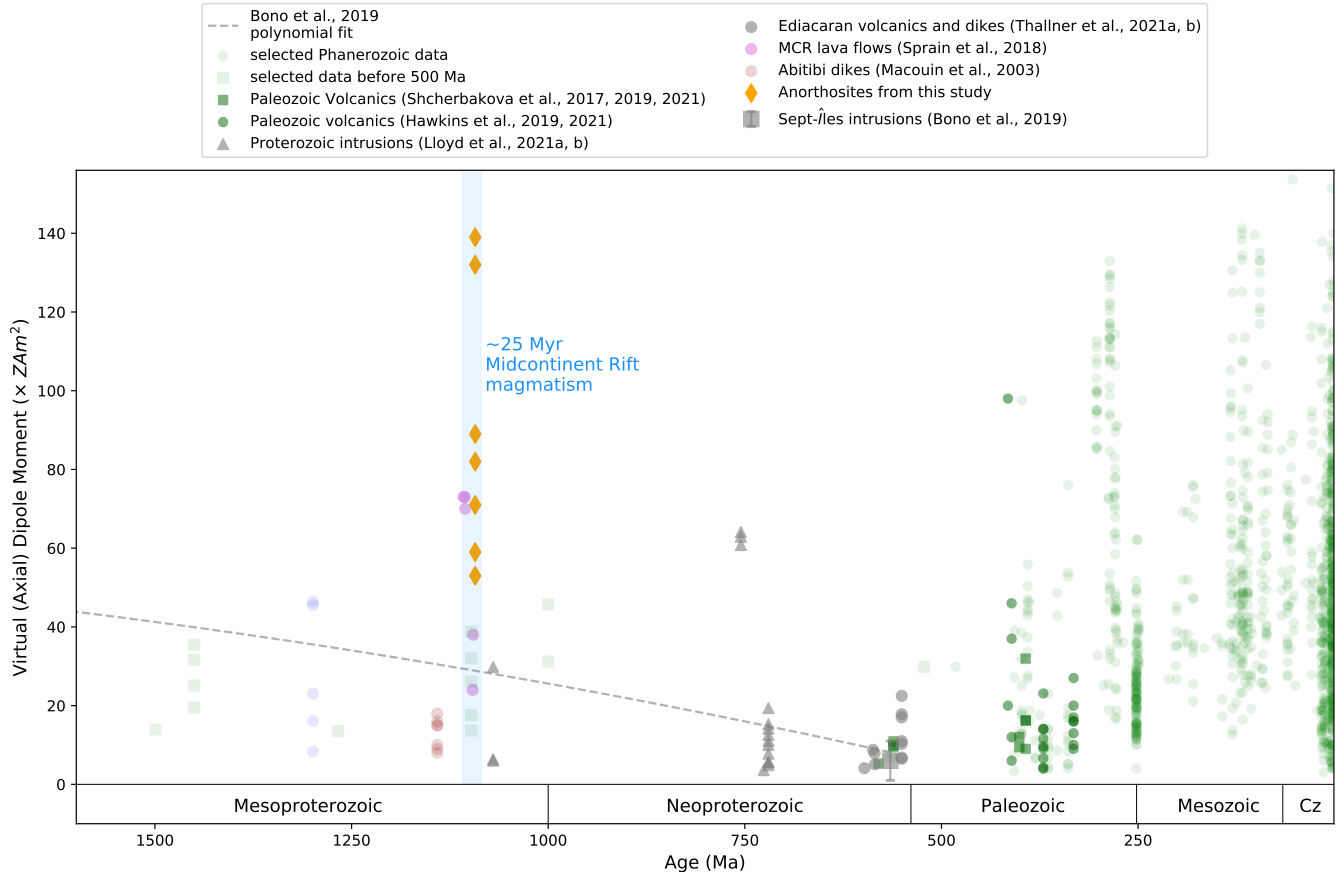


Fig. 6. Compilation of calculated virtual (axial) dipole moment values from the PINT database (PINT v8.0.0; <http://www.pintdb.org/>; 44), including all Phanerozoic VDM and VADM records with Q_{Pf} values >3 and additional Neoproterozoic data from refs. 17, 45–47. Paleointensity estimates from (21) and (22) are not included in the compilation due to the specimen-level double-slope behavior as discussed in the text. Overall the anorthosite xenoliths from this study record a high Mesoproterozoic field exceeding the value projected by the second order polynomial curve from (15) which is based on an interpretation of there being a monotonic decay of the geodynamo through the Proterozoic. The highest site-mean virtual dipole moment of the anorthosites are similar to the 99.5 percentile of the selected Phanerozoic data.

Abitibi dikes paleointensity estimates do not go to values as low as the Sept-Îles intrusions, this virtual dipole moment increase in the Mesoproterozoic is the largest yet documented in the Precambrian on a 10s of millions of years timescale (Fig. 6). The tempo and scale of this field intensity transition could match with model-based predictions associated with the onset of inner core nucleation (52). This timing would be broadly consistent with that proposed by 55. However, a model prediction of sustained strong field values following inner core nucleation is challenged by data from the ca. 1070 Ma Bangemall Sills which include a sill with a low virtual dipole moment of ~ 6.4 ZAm 2 (Fig. 6; 46). Following the Ediacaran, there are also low paleointensity estimates from Devonian rocks such as ca. 370 Ma dikes and lavas of the Siberian Viluy Traps that give virtual dipole moment estimates of 4.3 to 14.9 ZAm 2 (Fig. 6; 60). These low values as well as data from the ca. 414 Ma Strathmore lava flows (20), the ca. 410–380 Ma lava flows of Siberia and the Kola Peninsula (18), the ca. 408–393 Ma Burabay volcanics (19) and the ca. 332 Ma Kinghorn volcanics (20) has led to the proposal of this interval as the “Mid-Paleozoic Dipole Low” (20). This “Mid-Paleozoic Dipole Low” is followed by high paleointensity values such that there is a six-fold increase in the database from virtual dipole moment of ~ 16 ZAm 2 at ca. 332 Ma to ~ 99 ZAm 2 ca. 308 Ma in the late Carboniferous (Fig. 6; 20).

Given that the multiple records of a weak field can not all be a minimum prior to inner core nucleation, what processes could lead to a weak dipole at Earth’s surface even in the presence of a crystallizing inner core? Numerical models have shown that the dipole moment is sensitive to both the magnitude and spatial pattern of heat flow across the core-mantle boundary when there are strong available power sources to the geodynamo (61, 62). In such models, relatively low total heat flux across the core-mantle boundary can prevent the axial dipole from reversing whereas a high heat flux through the boundary can result in an increase in reversal frequency and decrease in dipole intensity. The “Mid-Paleozoic Dipole Low” has been hypothesized to be the result of such elevated core-mantle boundary heat flux conditions at a time when there was also available power from a crystallizing inner core (60), thereby also explaining the observed low paleointensities which include values as weak as those of the ca. 565 Ma Sept-Îles intrusions (Fig. 6; 15). Mantle convection can modulate core mantle boundary heat flow through changes in the structure of the deep mantle associated with upwelling plumes (63, 64) and subducted slabs (65–67). Strong evidence for differential plate tectonic motion extends back to ca. 2.2 Ga in the Paleoproterozoic (68, 69) and potentially back to ca. 3.2 Ga in the Archean (4). Plate tectonic modulations of core mantle boundary heat flow are therefore expected throughout

487 the Proterozoic. Such changes may explain large variability
488 in Proterozoic paleointensity values similar to those seen in
489 the Phanerozoic (45) and may challenge our ability to detect
490 the increase in surface geomagnetic field strength predicted to
491 have happened at the onset of inner core crystallization.

492 Overall, the high-fidelity paleointensity recorders of the
493 Beaver River anorthosite xenoliths in the well-preserved Mid-
494 continent Rift record strong field strengths 1.1 billion years
495 ago. The highest site-level value of the virtual dipole moment
496 would rank in the top 1% of those in the database for the
497 Cenozoic Era (the last 66 million years) when there was un-
498 equivocally a crystallizing inner core. These high surface field
499 strengths necessitate appreciable power to the late Mesopro-
500 terozoic geodynamo.

501 Materials and Methods

502

503 **Sample collection and paleomagnetic directions.** We collected paleo-
504 magnetic cores that are 2.5 cm in diameter along the southern and
505 eastern Beaver Bay Complex with a particular focus on acquiring
506 paired sites of anorthosite xenoliths and their local diabase hosts
507 during summer field seasons in 2019 and 2020. Sample cores were
508 collected using a hand-held gasoline-powered drill and were oriented
509 using a magnetic compass as well as a sun compass when possible.
510 Sun compass orientations were preferentially used for determining
511 the sample azimuth. Sister specimens underwent step-wise alter-
512 nating field (AF) or thermal demagnetization at the UC Berkeley
513 Paleomagnetism Lab to isolate paleomagnetic directions (data pre-
514 sented in (27)). Based on the anorthosite thermal demagnetization
515 results, we selected sites whose unblocking temperature ranges are
516 narrow and near 580°C for paleointensity experiments. Beaver River
517 diabase sites with minimal secondary remanence were also selected
518 for paleointensity experiments.

519 **Paleointensity experiment.** A total of 86 specimens from 14
520 anorthosite xenoliths and a total of 69 specimens from 7 diabase sites
521 underwent paleointensity experiments that followed the step-wise
522 double-heating Thellier method (70) using the IZZI protocol (26)
523 with heating steps up to 585 °C. Partial thermal remanent magneti-
524 zation (pTRM) checks were performed systematically throughout
525 the experiment to test whether there was significant mineralogical
526 alteration due to heating and were assessed using the SCAT param-
527 eter of (71). On top of the IZZI-Thellier experiment protocol, we also
528 performed a comparative study where we added an extra step of 20
529 mT alternating field (AF) cleaning on some of the specimens after
530 each in-field step. The purpose is to study whether the AF cleaning
531 could help improve experiment success rate by removing the rema-
532 nence component carried by materials such as multi-domain (MD)
533 grains that contribute to non-ideal paleointensity behaviors. The
534 results were similar when this step was applied without an observed
535 change in experimental success rate. All remanence measurements
536 were made on a 2G Enterprises DC-SQUID superconducting rock
537 magnetometer equipped with an automated sample changer system
538 at the UC Berkeley Paleomagnetism laboratory. The magnetometer
539 is housed inside a three-layer magnetostatic shield that maintains
540 background fields of less than 500 nT. Heating steps were performed
541 using an ASC TD-48SC thermal demagnetizer with a controlled
542 field coil that allows for a magnetic field to be generated in the oven
543 in conjunction with a DC power supply. The thermal demagnetizer
544 was degaussed with an alternating field in the axial orientation
545 following each in-field step such that residual fields within the oven
546 were <10 nT during zero-field steps. Samples were placed in the
547 same location within the thermal demagnetizer for each heating
548 step and were maintained in the same orientation with regard to
549 the applied field. During each heating step, the oven remained at
550 peak temperatures for 20 min to make sure each specimen reached
551 the target temperature. An applied laboratory field of 30 µT was
552 used for all in-field steps. All heating steps were performed in air.
553 The temperature increments for the experiments were chosen to
554 isolate magnetizations held by (titano)magnetite informed by the

555 previous demagnetization data, with smaller increments performed
556 close to the expected unblocking temperature of ~580°C.

557 **Paleointensity result selection.** The following criteria were used as
558 quality filters on the paleointensity results: (1) a maximum angular
559 deviation (MAD; 72) of <20°; (2) scatter parameter (β ; 73) values
560 of <15%; (3) a deviation angle (DANG; 74) of <5°; (4) fraction of
561 remanence fitted for paleointensity estimate (FRAC; (71)) >0.6; (5)
562 scatter statistic (SCAT; 71) = TRUE; (6) a maximum magnetic
563 moment difference between adjacent zero-field steps (GAP-Max;
564 71) < 0.25; (7) number of pTRM checks > 2; (8) and number of
565 measurements used for paleointensity determination ≥ 4. The MAD
566 measures the scatter about the best-fit line through the natural
567 remanent magnetization (NRM) steps in the selected interval for
568 which the intensity is defined. DANG, the deviation angle, is the
569 angle between the best-fit direction that is free floating and the
570 direction between the centre of mass of the data and the origin of the
571 vector component diagram (74). Both MAD and DANG assess the
572 directional variation of the NRM, with MAD measuring the scatter
573 in the NRM directions and DANG assessing whether the component
574 is trending toward the origin of the Zijderveld plot. β is the "scatter"
575 parameter of (73) and is the ratio of the standard error of the slope
576 of the best-fit line of the selected NRM and pTRM points on an
577 NRM/TRM plot to the absolute value of the slope. FRAC is the
578 value was chosen to preferentially select samples with dominantly
579 single-slope NRM/TRM plots. GAP-Max is the maximum gap
580 between two points on the NRM/TRM plot determined by vector
581 arithmetic. SCAT is a Boolean operator which uses the error on
582 the best-fit slope of the selected data on the NRM/TRM plot to
583 determine if the data are overly scattered. The parameter is used
584 to assess pTRM checks in addition to assessing the degree to which
585 IZZI steps are zigzagged. β , FRAC, GAP-Max and SCAT are
586 all statistics to assess the behavior of NRM/TRM plots. See the
587 Standard Paleointensity Definitions (75; <https://earthorg/PmagPy/SPD/home.html>) for more details. Data analysis was conducted using
588 Thellier GUI (71) within the PmagPy software package (76).

589 **Rock magnetic experiments.** We conducted rock magnetic experiments
590 with a purpose of gaining magnetic mineralogy insights into the
591 paleointensity results of the anorthosite and diabase. Back-
592 field curves were measured at room temperature using a Micromag
593 Princeton Measurements vibrating sample magnetometer (VSM)
594 and a Lake Shore 8600 series VSM at the Institute for Rock Mag-
595 netism. Specimen median destructive fields (MDF) are calculated
596 based on the backfield curves. The calculated coercivity spectra
597 were subsequently decomposed into one or more components using
598 skew-normal distributions following the method of (40) examples of
599 which are shown in Fig. 5. We also used a magnetic property
600 measurement system (MPMS) at the Institute for Rock Magnetism
601 to aid in the identification of magnetic minerals. In the field-cooled
602 (FC) experiments, specimen magnetizations were measured upon
603 warming following the specimen having cooled in an applied field of
604 2.5 T from 300 to 10 K. In the zero-field-cooled (ZFC) experiment,
605 a low-temperature saturation isothermal remanence (LTSIRM) of
606 2.5 T was applied at 10 K after the specimen cooled in a (near-)zero
607 field. In the room-temperature saturation isothermal remanence
608 (RTSIRM) experiment, the sample was pulsed with a 2.5 T field at
609 room temperature (~300 K) and then cooled to 10 K and warmed
610 back to room temperature in a (near-)zero field. The magnetic moment
611 transitions at critical temperatures revealed through MPMS
612 experiments are used to identify magnetic minerals such as mag-
613 netite within specimens (38).

614 To further identify the magnetic carriers within the Beaver River
615 anorthosite xenoliths and compare them with the anorthosites of
616 the Duluth Complex Anorthositic Series rocks, we used the quan-
617 tum diamond microscope (QDM) at the UC Berkeley Paleomag-
618 netism laboratory to image a thin section of sample MS99033 from
619 anorthosite xenolith AX16 (which yielded a $^{206}\text{Pb}/^{238}\text{U}$ zircon date
620 of 1091.83 ± 0.21 Ma; (27)), and a thin section of a Duluth Complex
621 anorthosite (Fig. 2). We use the QDM to image the magnetic field
622 over the polished thin section surfaces with a sample-sensor distance
623 of 5 μm in projective magnetic microscopy (PMM) mode with a
624

626 spatial resolution of 4.7 m per pixel and an instantaneous 0.9 mT
627 bias field that is canceled during the course of measurement (77).

628 **ACKNOWLEDGMENTS.** Project research was supported by NSF
629 CAREER grant EAR-1847277 to N.L.S.-H., an Institute on Lake
630 Superior Geology Student Research Fund grant to Y.Z., and an
631 Institute for Rock Magnetism Visiting Student Fellowship to Y.Z.
632 The Institute for Rock Magnetism is supported by the Instrumentation
633 and Facilities program of the NSF Earth Science Division.
634 Permits for fieldwork and sampling from the Minnesota Department
635 of Natural Resources are gratefully acknowledged. We thank James
636 Pierce and Blake Hodgin for their assistance in the field. We thank
637 Jim Miller for providing us with the Duluth Complex anorthosites
638 thin section. We thank Dario Bilardello, Peat Solheid, Mike Jackson,
639 Josh Feinberg, and Bruce Moskowitz for their tremendous help associated
640 with instrument operation, data interpretations, and research
641 guidance at the IRM. Conversations with Bruce Buffett and Zachary
642 Geballe informed our perspectives on the geodynamic and mineral
643 physics literature. Paleomagnetic data associated with this study
644 are available within the Magic database (<https://earthorg/MagIC/19462/8d3c2258-11ae-4830-b99f-3fb02eceb7e>; provide link when doi is generated at time of proofs) and all data are within a Github repository along with Python code related to calculations and visualizations (https://github.com/Swanson-Hysell-Group/AX_BD_PINT) that are also archived on Zenodo (provide link when doi is generated at time of proofs).

- 51 1. BA Buffett, Earth's core and the geodynamo. *Science* **288**, 2007–2012 (2000).
- 52 2. P Selkin, J Gee, L Tauxe, Nonlinear thermoremanence acquisition and implications for paleointensity data. *Earth Planet. Sci. Lett.* **256**, 81–89 (2007).
- 53 3. JA Tarduno, EG Blackman, EE Mamajek, Detecting the oldest geodynamo and attendant shielding from the solar wind: Implications for habitability. *Phys. Earth Planet. Interiors* **233**, 68–87 (2014).
- 54 4. AR Brenner, et al., Paleomagnetic evidence for modern-like plate motion velocities at 3.2 Ga. *Ga. Sci. Adv.* **6**, eaaz8670 (2020).
- 55 5. CJ Davies, M Pozzo, D Gubbins, D Alfè, Constraints from material properties on the dynamics and evolution of Earth's core. *Geophys. J. Int.* **8**, 678–685 (2015).
- 56 6. D Gubbins, D Alfè, G Masters, GD Price, M Gillan, Gross thermodynamics of two-component core convection. *Geophys. J. Int.* **157**, 1407–1414 (2004).
- 57 7. Z Konopková, RS McWilliams, N Gómez-Pérez, AF Goncharov, Direct measurement of thermal conductivity in solid iron at planetary core conditions. *Nature* **534**, 99–101 (2016).
- 58 8. M Pozzo, C Davies, D Gubbins, D Alfè, Thermal and electrical conductivity of iron at Earth's core conditions. *Nature* **485**, 355–358 (2012).
- 59 9. N de Koker, G Steinle-Neumann, V Vlcek, Electrical resistivity and thermal conductivity of liquid Fe alloys at high P and T, and heat flux in Earth's core. *Geophys. J. Int.* **109**, 4070–4073 (2012).
- 60 10. H Gomi, et al., The high conductivity of iron and thermal evolution of the Earth's core. *Phys. Earth Planet. Interiors* **224**, 88–103 (2013).
- 61 11. Y Zhang, et al., Reconciliation of experiments and theory on transport properties of iron and the geodynamo. *Nature* **125** (2020).
- 62 12. S Labrosse, Thermal evolution of the core with a high thermal conductivity. *Phys. Earth Planet. Interiors* **247**, 36–55 (2015).
- 63 13. K Ohta, Y Kuwayama, K Hirose, K Shimizu, Y Ohishi, Experimental determination of the electrical resistivity of iron at Earth's core conditions. *Nature* **534**, 95–98 (2016).
- 64 14. NL Swanson-Hysell, The Precambrian paleogeography of Laurentia in *Ancient Supercontinents and the Paleogeography of Earth*. (Elsevier), pp. 109–153 (2021).
- 65 15. RK Bono, JA Tarduno, F Nimmo, RD Cottrell, Young inner core inferred from Ediacaran ultralow geomagnetic field intensity. *Nat. Geosci.* **12**, 143–147 (2019).
- 66 16. VV Shcherbakova, et al., Ultra-low palaeointensities from East European Craton, Ukraine support a globally anomalous palaeomagnetic field in the Ediacaran. *Geophys. J. Int.* **220**, 1928–1946 (2019).
- 67 17. D Thallner, AJ Biggin, HC Halls, An extended period of extremely weak geomagnetic field suggested by palaeointensities from the Ediacaran Grenville dykes (SE Canada). *Earth Planet. Sci. Lett.* **568**, 117025 (2021).
- 68 18. VV Shcherbakova, et al., Was the Devonian geomagnetic field dipolar or multipolar? Palaeointensity studies of Devonian igneous rocks from the Minusa Basin (Siberia) and the Kola Peninsula dykes, Russia. *Geophys. J. Int.* **209**, 1265–1286 (2017).
- 69 19. VV Shcherbakova, et al., Ultra-Low Geomagnetic Field Intensity in the Devonian Obtained from the Southern Ural Rock Studies. *Izvestiya, Phys. Solid Earth* **57**, 900–912 (2021).
- 70 20. LMA Hawkins, et al., Intensity of the Earth's magnetic field: Evidence for a Mid-Paleozoic dipole low. *Proc. Natl. Acad. Sci.* **118**, e2017342118 (2021).
- 71 21. LJ Pesonen, HC Halls, Geomagnetic field intensity and reversal asymmetry in late Precambrian Keweenawan rocks. *Geophys. J. Int.* **73**, 241–270 (1983).
- 72 22. EV Kulakov, AV Smirnov, Jr Diehl, Absolute geomagnetic paleointensity as recorded by ~1.09 Ga Lake Shore Traps (Keweenaw Peninsula, Michigan). *Studia Geophys. et Geod.* **57**, 565–584 (2013).
- 73 23. CJ Sprain, NL Swanson-Hysell, LM Fairchild, K Gaastra, A field like today's? The strength of the geomagnetic field 1.1 billion years ago. *Geophys. J. Int.* **213**, 1969–1983 (2018).
- 74 24. J Kasbohm, B Schoene, S Burgess, Radiometric constraints on the timing, tempo, and effects of large igneous province emplacement (2021).
- 75 25. NL Swanson-Hysell, J Ramezani, LM Fairchild, IR Rose, Failed rifting and fast drifting: Mid-continent Rift development, Laurentia's rapid motion and the driver of Grenvillian orogenesis. *GSA Bull.* **131**, 913–940 (2019).
- 76 26. Y Yu, L Tauxe, A Genevey, Toward an optimal geomagnetic field intensity determination technique. *Geochem. Geophys. Geosystems* **5** (2004).
- 77 27. Y Zhang, NL Swanson-Hysell, MD Schmitz, JD Miller, MS Avery, Synchronous emplacement of the anorthosite xenolith-bearing Beaver River diabase and one of the largest lava flows on Earth. *Geochem. Geophys. Geosystems* (2021).
- 78 28. TJ Boerboom, M-147 Bedrock geology of the Split Rock Point quadrangle, Lake County, Minnesota, (Minnesota Geological Survey), Technical report (2004).
- 79 29. TJ Boerboom, JC Green, P Albers, J Miller, J.D., M-171 Bedrock geology of the Tofte quadrangle, Cook County, Minnesota, (Minnesota Geological Survey), Technical report (2006).
- 80 30. J Miller, J.D., PW Weiblen, Anorthositic rocks of the Duluth Complex: Examples of rocks formed from plagioclase crystal mush. *J. Petrol.* **31**, 295–339 (1990).
- 81 31. N Scofield, WM Roggenten, Petrologic evolution of plagioclase-rich cumulates from the Wichita Mountains, Oklahoma: Effects upon magnetic remanence properties. *Geology* **14**, 908 (1986).
- 82 32. P Selkin, J Gee, L Tauxe, W Meurer, A Newell, The effect of remanence anisotropy on paleointensity estimates: a case study from the Archean Stillwater Complex. *Earth Planet. Sci. Lett.* **183**, 403–416 (2000).
- 83 33. JM Feinberg, HR Wenk, GR Scott, PR Renne, Preferred orientation and anisotropy of seismic and magnetic properties in gabbroites from the Bushveld layered intrusion. *Tectonophysics* **420**, 345–356 (2006).
- 84 34. AJ Biggin, GA Paterson, A new set of qualitative reliability criteria to aid inferences on palaeomagnetic dipole moment variations through geological time. *Front. Earth Sci.* **2** (2014).
- 85 35. B Cyph, M Morzfeld, L Tauxe, Bias corrected estimation of paleointensity (BiCEP): An improved methodology for obtaining paleointensity estimates. *Geochem. Geophys. Geosystems* **22** (2021).
- 86 36. GA Paterson, A simple test for the presence of multidomain behavior during paleointensity experiments. *J. Geophys. Res.* **116** (2011).
- 87 37. EJW Verwey, Electronic Conduction of Magnetite (Fe₃O₄) and its Transition Point at Low Temperatures. *Nature* **144**, 327–328 (1939).
- 88 38. JM Feinberg, PA Solheid, NL Swanson-Hysell, MJ Jackson, JA Bowles, Full vector low-temperature magnetic measurements of geologic materials. *Geochem. Geophys. Geosystems* **16**, 301–314 (2015).
- 89 39. Ö Özdemir, DJ Dunlop, BM Moskowitz, The effect of oxidation on the Verwey transition in magnetite. *Geophys. Res. Lett.* **20**, 1671–1674 (1993).
- 90 40. DP Maxbauer, JM Feinberg, DL Fox, MAX UnMix: A web application for unmixing magnetic coercivity distributions. *Comput. Geosci.* **95**, 140–145 (2016).
- 91 41. MH Dodson, E McClelland-Brown, Magnetic blocking temperatures of single-domain grains during slow cooling. *J. Geophys. Res.* **85**, 2625 (1980).
- 92 42. SL Halgedahl, R Day, M Fuller, The effect of cooling rate on the intensity of weak-field trm in single-domain magnetite. *J. Geophys. Res. Solid Earth* **85**, 3690–3698 (1980).
- 93 43. L Nagy, W Williams, L Tauxe, Estimating the effect of cooling rate on the acquisition of magnetic remanence. *Geophys. Res. Lett.* **48** (2021).
- 94 44. RK Bono, et al., The PINT database: A definitive compilation of absolute palaeomagnetic intensity determinations since 4 billion years ago. *Geophys. J. Int.* (2021).
- 95 45. SJ Lloyd, AJ Biggin, H Halls, MJ Hill, First Palaeointensity Data from the Cryogenian and their potential implications for Inner Core Nucleation Age. *Geophys. J. Int.* (2021).
- 96 46. SJ Lloyd, AJ Biggin, ZX Li, New paleointensity data suggest possible Phanerozoic-type palaeomagnetic variations in the Precambrian. *Geochem. Geophys. Geosystems* (2021).
- 97 47. D Thallner, AJ Biggin, PJA McCausland, RR Fu, New paleointensities from the Skinner Cove Formation, Newfoundland, suggest a changing state of the geomagnetic field at the Ediacaran-Cambrian transition. *J. Geophys. Res. Solid Earth* (2021).
- 98 48. K Ohta, K Hirose, The thermal conductivity of the Earth's core and implications for its thermal and compositional evolution. *Natl. Sci. Rev.* **8** (2021).
- 99 49. F Stacey, D Loper, A revised estimate of the conductivity of iron alloy at high pressure and implications for the core energy balance. *Phys. Earth Planet. Interiors* **161**, 13–18 (2007).
- 100 50. WP Hsieh, et al., Low thermal conductivity of iron-silicon alloys at Earth's core conditions with implications for the geodynamo. *Nat. Commun.* **11** (2020).
- 101 51. Q Williams, The thermal conductivity of Earth's core: a key geophysical parameter's constraints and uncertainties. *Annu. Rev. Earth Planet. Sci.* **46**, 47–66 (2018).
- 102 52. CJ Davies, et al., Dynamo constraints on the long-term evolution of Earth's magnetic field strength. *Geophys. J. Int.* (2021).
- 103 53. J Aubert, Stéphane, C Poitou, Modelling the palaeo-evolution of the geodynamo. *Geophys. J. Int.* **179**, 1414–1428 (2009).
- 104 54. M Landeau, J Aubert, P Olson, The signature of inner-core nucleation on the geodynamo. *Earth Planet. Sci. Lett.* **465**, 193–204 (2017).
- 105 55. AJ Biggin, et al., Palaeomagnetic field intensity variations suggest Mesoproterozoic inner-core nucleation. *Nature* **526**, 245–248 (2015).
- 106 56. HC Halls, A Lovette, M Hamilton, U Söderlund, A paleomagnetic and U–Pb geochronology study of the western end of the Grenville dyke swarm: Rapid changes in paleomagnetic field direction at ca. 585 Ma related to polarity reversals? *Precambrian Res.* **257**, 137–166 (2015).
- 107 57. KP Kodama, Combined magnetostratigraphy from three localities of the Rainstorm Member of the Johnnie Formation in California and Nevada, United States Calibrated by Cyclostratigraphy: A 13 R/Ma Reversal Frequency for the Ediacaran. *Front. Earth Sci.* **9** (2021).
- 108 58. PE Driscoll, Simulating 2 Ga of geodynamo history. *Geophys. Res. Lett.* **43**, 5680–5687 (2016).
- 109 59. M Macouin, et al., Low paleointensities recorded in 1 to 2.4 Ga Proterozoic dykes, Superior Province, Canada. *Earth Planet. Sci. Lett.* **213**, 79–95 (2003).
- 110 60. L Hawkins, et al., An exceptionally weak Devonian geomagnetic field recorded by the Viluy Traps, Siberia. *Earth Planet. Sci. Lett.* **506**, 134–145 (2019).
- 111 61. P Olson, Gravitational dynamos and the low-frequency geomagnetic secular variation. *Proc. Natl. Acad. Sci.* **104**, 20159–20166 (2007).
- 112 62. PL Olson, RS Coe, PE Driscoll, GA Glatzmaier, PH Roberts, Geodynamo reversal frequency

- 788 and heterogeneous core–mantle boundary heat flow. *Phys. Earth Planet. Interiors* **180**, 66–
789 79 (2010).
- 790 63. RL Larson, P Olson, Mantle plumes control magnetic reversal frequency. *Earth Planet. Sci.*
791 *Lett.* **107**, 437–447 (1991).
- 792 64. V Courtillot, P Olson, Mantle plumes link magnetic superchrons to Phanerozoic mass deple-
793 tion events. *Earth Planet. Sci. Lett.* **260**, 495–504 (2007).
- 794 65. E Tan, M Gurnis, L Han, Slabs in the lower mantle and their modulation of plume formation.
795 *Geochem. Geophys. Geosystems* **3**, 1–24 (2002).
- 796 66. AJ Biggin, et al., Possible links between long-term geomagnetic variations and whole-mantle
797 convection processes. *Nat. Geosci.* **5**, 526–533 (2012).
- 798 67. MW Hounslow, M Domeier, AJ Biggin, Subduction flux modulates the geomagnetic polarity
799 reversal rate. *Tectonophysics* **742–743**, 34–49 (2018).
- 800 68. RN Mitchell, et al., Plate tectonics before 2.0 Ga: Evidence from paleomagnetism of cratons
801 within supercontinent Nuna. *Am. J. Sci.* **314**, 878–894 (2014).
- 802 69. NL Swanson-Hysell, et al., The paleogeography of Laurentia in its early years: new constraints
803 from the paleoproterozoic east-central Minnesota batholith. *Tectonics* (2021).
- 804 70. O Thellier, E.; Thellier, Sur l'intensité du champ magnétique terrestre dans le passé historique
805 et géologique. *Annales de Géophys.* **15**, 285–378 (1959).
- 806 71. R Shaar, L Tauxe, Thellier GUI: An integrated tool for analyzing paleointensity data from
807 Thellier-type experiments. *Geochem. Geophys. Geosystems* **14**, 677–692 (2013).
- 808 72. JL Kirschvink, The least-squares line and plane and the analysis of palaeomagnetic data.
809 *Geophys. J. Int.* **62**, 699–718 (1980).
- 810 73. RS Coe, S Grommé, EA Mankinen, Geomagnetic paleointensities from radiocarbon-dated
811 lava flows on Hawaii and the question of the Pacific nondipole low. *J. Geophys. Res. Solid
812 Earth* **83**, 1740–1756 (1978).
- 813 74. L Tauxe, H Staudigel, Strength of the geomagnetic field in the Cretaceous Normal Super-
814 chron: New data from submarine basaltic glass of the Troodos Ophiolite. *Geochem. Geophys.
815 Geosystems* **5** (2004).
- 816 75. GA Paterson, L Tauxe, AJ Biggin, R Shaar, LC Jonestrask, On improving the selection of
817 Thellier-type paleointensity data. *Geochem. Geophys. Geosystems* **15**, 1180–1192 (2014).
- 818 76. L Tauxe, et al., PmagPy: Software package for paleomagnetic data analysis and a bridge to
819 the Magnetics Information Consortium (MagIC) Database. *Geochem. Geophys. Geosystems*
820 **17**, 2450–2463 (2016).
- 821 77. DR Glenn, et al., Micrometer-scale magnetic imaging of geological samples using a quantum
822 diamond microscope. *Geochem. Geophys. Geosystems* **18**, 3254–3267 (2017).